Journal of Materials Chemistry A

PAPER

View Article Online
View Journal | View Issue

Cite this: J. Mater. Chem. A, 2019, 7, 15233

Threshold catalytic onset of carbon formation on CeO_2 during CO_2 electrolysis: mechanism and inhibition†

Jiayue Wang,[a] Sean R. Bishop,‡[b] Lixin Sun,[a] Qiyang Lu,[c] Gulin Vardar,[a] Roland Bliem,[a] Nikolai Tsvetkov,[a] Ethan J. Crumlin,[d] Jean-Jacques Gallet,[ef] Fabrice Bournel,[ef] Iradwikanari Waluyo[g] and Bilge Yildiz*[ac]

Carbon deposition from CO and other carbon-containing fuels is a major cause of the performance degradation of catalysts and electrocatalysts in many energy conversion devices, including low-temperature solid oxide cells (LT-SOCs). In this work, we present direct observation of carbon deposition on thin-film CeO_2 electrodes at LT-SOC operating temperatures (450 °C) in a CO/CO_2 atmosphere by *in operando* X-ray photoelectron spectroscopy. In contrast to the general view that CeO_2 is a carbon tolerant material, significant carbon formation was observed on CeO_2 during CO_2 electrolysis, with no other catalyst present. Moreover, carbon deposition on CeO_2 demonstrated an intriguing threshold onset formation against surface Ce^{3+} concentration. With the aid of Monte Carlo simulations, we propose the neighboring Ce^{3+}–Ce^{3+} pairs to be a critical catalytic structure that facilitates carbon deposition from CO. Finally, we propose mitigation of carbon deposition on CeO_2 by doping CeO_2 with non-redox-active cations, and proved this concept using 50% Gd- and 50% Zr-doped CeO_2 as an example system. These findings provide an in-depth understanding of the mechanism of carbon deposition on CeO_2 during electrochemical reactions and can guide the design of carbon-resistant CeO_2-based electrocatalysts.

Received 15th April 2019
Accepted 22nd May 2019

DOI: 10.1039/c9ta03265g

rsc.li/materials-a

Introduction

To produce carbon-neutral fuels,[1,2] environmentally friendly technologies, including electrolysis[3] and thermochemical splitting[4] of water and carbon dioxide, have attracted significant attention. In particular, low-temperature solid oxide cells (LT-SOC) that operate from 400 °C to 650 °C are believed to be the next generation technology.[5,6] However, carbon poisoning, or "coking", due to carbon deposition on the catalyst surface during operation, is an important issue for processes involving carbon-containing species.[7,8] This coking process can lead to irreversible catalyst deactivation and cause mechanical degradation.[9] One major type of carbon poisoning is from CO,[10–14] which has been reported as either CO dissociation[15,16] ($CO \rightarrow C + O$) or the Boudouard disproportionation[17–19] ($2CO \rightarrow CO_2 + C$). At operating temperatures below 700 °C, carbon deposition is thermodynamically more favorable and occurs mainly *via* the Boudouard reaction.[5,20] Consequently, it is important to develop carbon-tolerant electrocatalysts that can operate under LT-SOC operating conditions, with both high catalytic activity and long-term stability.

Ceria (CeO_2) and ceria-based materials have been widely investigated as catalysts and catalyst supports towards a broad range of reactions.[21–23] The catalytic performance of CeO_2 is due to its excellent redox activity,[24] which can be expressed with the Kröger–Vink notation[25] as

$$2Ce_{Ce} + O_O \rightarrow 2Ce_{Ce}' + V_O^{\cdot\cdot} + \frac{1}{2}O_2, \quad (1)$$

where Ce_{Ce}' and $V_O^{\cdot\cdot}$ denote Ce^{3+} (small polaron[26]) and doubly positive charged oxygen vacancy, respectively. With this oxygen storage capability, CeO_2-based catalysts are also known to be carbon-tolerant as they can oxidize the deposited carbon with lattice oxygen.[27]

LT-SOC fuel electrodes combining ceria-based materials with Ni have yielded high performance but their stability in

[a]Department of Nuclear Science and Engineering, Massachusetts Institute of Technology (MIT), Cambridge, USA. E-mail: byildiz@mit.edu
[b]Materials Processing Center, MIT, Cambridge, MA, USA
[c]Department of Materials Science and Engineering, MIT, Cambridge, MA, USA
[d]Advanced Light Source, Lawrence Berkeley National Laboratory, Berkeley, CA, USA
[e]Sorbonne Université, CNRS, Laboratoire de Chimie Physique Matière et Rayonnement – Campus Pierre et Marie Curie, F-75005 Paris, France
[f]Synchrotron SOLEIL, L'Orme des Merisiers, Saint-Aubin, F-91192 Gif-sur-Yvette, France
[g]National Synchrotron Light Source II, Brookhaven National Laboratory, Upton, NY, USA

† Electronic supplementary information (ESI) available. See DOI: 10.1039/c9ta03265g

‡ Present Address: Redox Power Systems, LLC, College Park, MD, USA.

carbon-containing fuels remains a big challenge.[5,28] While carbon deposition has been extensively studied on the Ni surfaces, few studies focus on carbon deposition on CeO_2. Despite the high carbon tolerance of CeO_2 as a catalyst, carbon deposition may not be negligible on CeO_2 in LT-SOCs since the oxygen ion current can greatly affect the carbon tolerance of electrode materials.[29] In particular, in electrolysis conditions, O^{2-} are constantly removed from the fuel electrode, making carbon deposition more favorable.[30] As an example, recent studies have demonstrated that infiltrating Ni-YSZ with Gd-doped CeO_2 did not improve the carbon tolerance during CO_2 electrolysis.[31,32] Therefore, to obtain a more complete picture of carbon deposition over Ni/CeO_2 electrodes, it is important to investigate the onset of carbon formation and carbon deposition mechanism on CeO_2 during electrochemical reactions. Moreover, besides Ni/CeO_2 electrodes, there has been considerable development of CeO_2/perovskite fuel electrodes in LT-SOCs, as a means to improve the electrodes ability to work with carbon-containing fuels without carbon deposition.[5,33] Hence a fundamental study of carbon deposition on CeO_2 surface would also benefit the design of these conducting-oxide electrodes.

In this work, we systematically studied carbon deposition in CO/CO_2 mixture on four types of fluorite-type ceria thin films: undoped ceria (CeO_2), 20% Gd-doped ceria ($Gd_{0.2}Ce_{0.8}O_{1.9}$), 50% Gd-doped and 50% Zr-doped ceria ($Gd_{0.5}Ce_{0.5}O_{1.75}$, $Zr_{0.5}Ce_{0.5}O_2$). Despite the general opinion that CeO_2 is a carbon-tolerant material, we demonstrated for the first time with *in operando* ambient pressure X-ray photoelectron spectroscopy (APXPS) that carbon is readily deposited on the CeO_2 surface within half an hour, under LT-SOC operating conditions (450 °C, CO/CO_2 atmosphere, ~1 V polarization). Moreover, with quantification of both [Ce^{3+}] and the amount of deposited carbon, we demonstrate an intriguing threshold [Ce^{3+}]-carbon relation for the onset of carbon formation on CeO_2. Combining APXPS data with Monte Carlo simulation, we propose the most likely catalytic reaction for carbon deposition from CO on CeO_2 to be the neighboring Ce^{3+}–Ce^{3+} pair. Finally, we propose doping CeO_2 with non-redox-active cations can effectively mitigate the carbon deposition on CeO_2 in the LT-

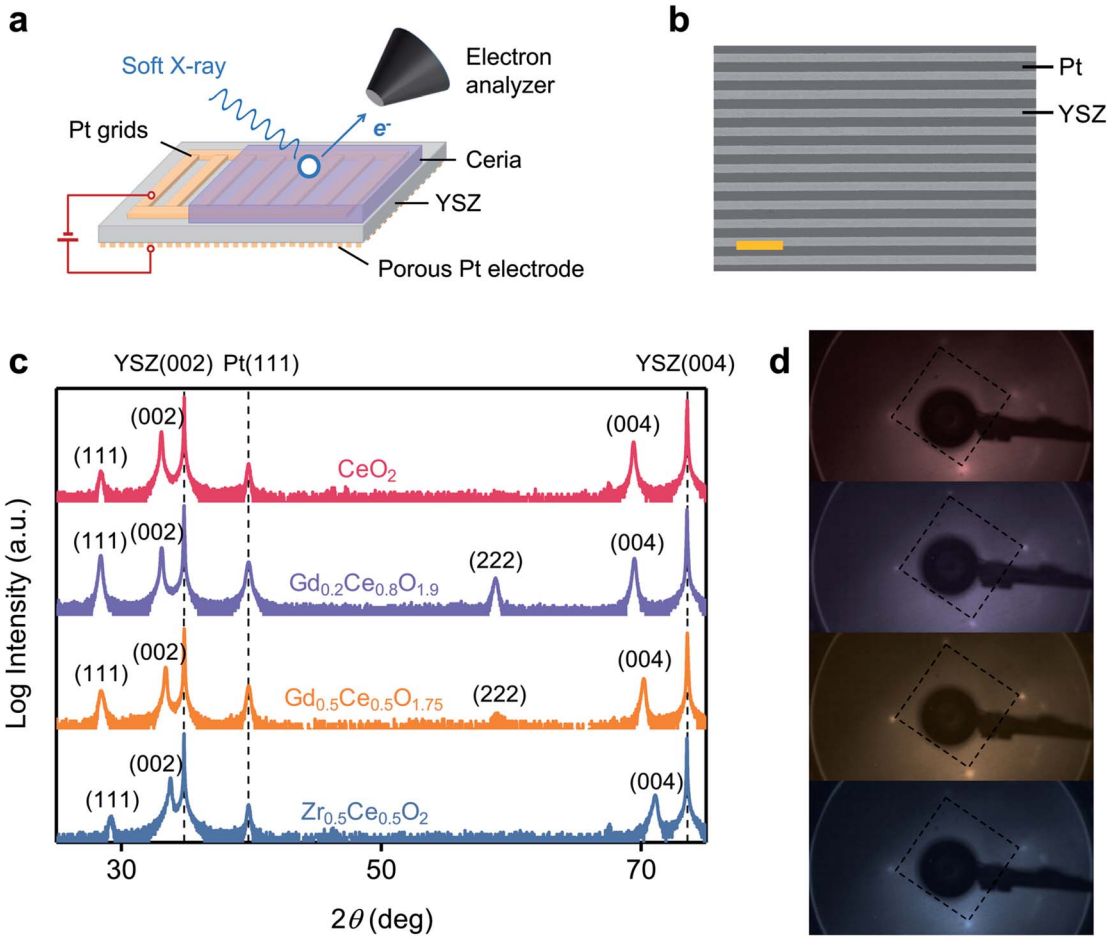

Fig. 1 Schematics of the experimental configuration and sample characterization. (a) The electrochemical cell consists of a thin-film ceria working electrode, a buried Pt grid, an 8% yttria-stabilized zirconia (YSZ) solid electrolyte, and a porous Pt counter electrode. (b) SEM image showing the patterned Pt grid; scale bar, 100 μm. (c) High-resolution X-ray diffraction data of symmetric 2θ-ω scan of the ceria thin-films on the electrochemical cell. (d) Low-energy electron diffraction patterns for the ceria thin films on YSZ (001) without Pt grids, collected at 450 °C in UHV using 110.6 eV electrons (color legends in (c)). A fourfold symmetry is present on all ceria electrodes, highlighted by the dashed square.

SOCs operating conditions, as exemplified in the case of $Gd_{0.5}Ce_{0.5}O_{1.75}$ and $Zr_{0.5}Ce_{0.5}O_2$.

Results

The experimental setup is shown in Fig. 1a and b, which depicts the electrochemical cell consisting of a ceria thin film electrode, an 8% yttria-stabilized zirconia (YSZ) (001) single crystal electrolyte, a Pt grid buried under the ceria electrodes, and a porous Pt counter electrode. The out-of-plane symmetric X-ray diffraction scan for the ceria films on the electrochemical cell is shown in Fig. 1c. The ceria films demonstrated both (001) and (111) orientations: the films grown epitaxially on YSZ are in the (001) direction while the polycrystalline regions grown on Pt grids follow a mixed (001) and (111) texture. Verification of this assignment is shown in ESI Fig. S2.† As explained in ESI Note 1,† all the ceria films have cubic fluorite structure (space group $Fm\bar{3}m$). To reveal the surface structure, low-energy electron diffraction (LEED) patterns were collected on ceria films epitaxially grown on YSZ (001) without Pt grids at 450 °C, *i.e.*, the same temperature where carbon deposition was studied. As shown in Fig. 1d, the surface of all the ceria thin films on YSZ (001) had a four-fold symmetry, in agreement with the (001) fluorite-type ceria surface structure.[24,34] On the other hand, the polycrystalline regions on the Pt grids have yielded no LEED pattern, consistent with previous reports.[24]

Fig. 2 summarizes the surface chemistry evolution during carbon deposition reaction. In the experiment, cathodic (CO_2

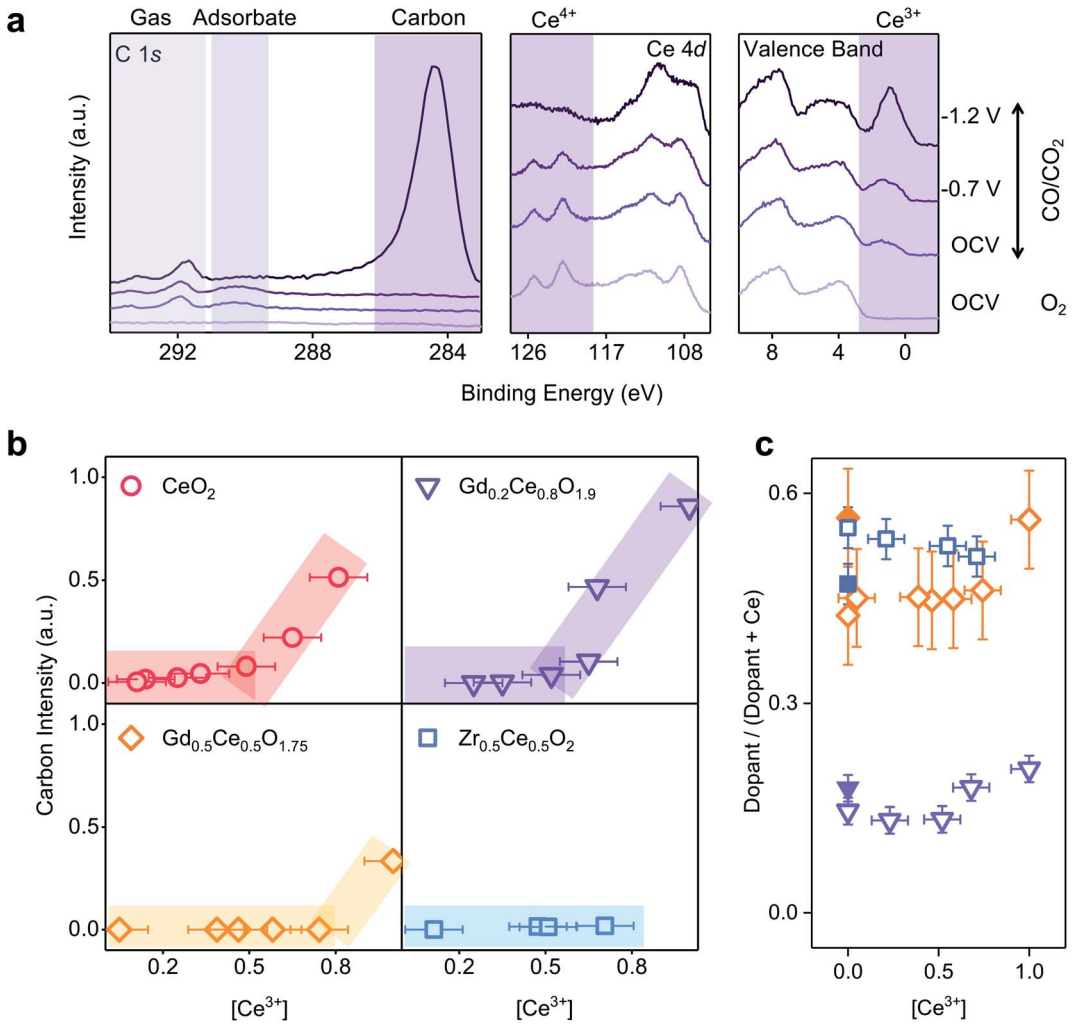

Fig. 2 Evolution of surface chemistry during carbon deposition. (a) C 1s, Ce 4d, and valence band as a function of applied electrochemical bias at 450 °C in 0.3 Torr 9 : 1 CO/CO_2 on $Gd_{0.2}Ce_{0.8}O_{1.9}$, with negative values representing cathodic polarization. The spectra taken at 350 °C in 0.02 Torr O_2 at OCV are shown as a reference. Both Ce 4d and valence band spectra indicate a more reduced surface under increasing cathodic bias. (b) The relation between carbon deposition and $[Ce^{3+}]$, where the color bands serve as a guide to the eye. Note the carbon intensity does not scale linearly with $[Ce^{3+}]$, instead the onset of significant carbon deposition is only after a threshold $[Ce^{3+}]$ on CeO_2 and on $Gd_{0.2}Ce_{0.8}O_{1.9}$. In addition, carbon deposition was significantly suppressed on both $Gd_{0.5}Ce_{0.5}O_{1.75}$ and $Zr_{0.5}Ce_{0.5}O_2$. (c) Surface cation composition as a function of $[Ce^{3+}]$. The open symbols represent the surface composition quantified by APXPS, with the points at $[Ce^{3+}] = 0$ showing the surface composition in O_2. The closed symbols at $[Ce^{3+}] = 0$ represent the as-prepared surface composition measured by lab-based XPS in UHV (legend in (b)).

reduction) and anodic (CO oxidation) biases were applied on the electrochemical cell. Since the width of Pt stripes (~20 μm) is much smaller than the X-ray spot size (~1 mm in diameter), the APXPS results reveal an average surface chemistry of the epitaxial and polycrystalline ceria regions. Fig. 2a shows the normalized C 1s, Ce 4d and valence band (VB) photoelectron spectra on $Gd_{0.2}Ce_{0.8}O_{1.9}$ as a representative case. All the spectra were calibrated by aligning the Ce $4d_{3/2}$ peaks at 122 eV[35,36] and then normalized to the Ce 4d intensity. Three main features were observed in the C 1s spectra. First, the pronounced rising peak at around 285 eV corresponds to the deposited graphitic carbon, in agreement with previous studies on carbon deposition on ceria.[37,38] Secondly, the peak at around 290 eV is an adsorbate peak, which has been commonly attributed to a carbonate species on the ceria surface.[36,38,39] Since a detailed investigation of the CO/CO_2 adsorption structure on ceria is beyond the scope of this paper, we leave this peak assigned as an adsorbate. Studies on this topic can be found in the ref. 40 and 41. Finally, the two peaks at around 292 eV and 293.5 eV originate from CO and CO_2 gas phase.[42,43] The assignment of the two gas peaks has been verified by collecting the C 1s spectra while the sample was extracted (ESI Fig. S6†).

The components with the two highest binding energies (shaded region in the plot) in the Ce 4d spectrum arise purely from Ce^{4+} species.[36,44] Note the Ce^{4+} features decreased under increasing cathodic polarization, indicating the reduction of ceria surface. In the valence band spectra, the feature at about 1.5 eV corresponds to the Ce 4f peak, whose normalized intensity reflects the concentration of Ce^{3+} at the surface.[36,45] Consistent with Ce 4d spectra, the valence band Ce 4f peak intensity increased with increased reduction state at the surface under cathodic polarization. As shown in Fig. 2a and ESI Fig. S7a,† surface $[Ce^{3+}]$ increased monotonically with cathodic polarization for all the ceria samples. At open circuit, both $Gd_{0.2}Ce_{0.8}O_{1.9}$ and $Zr_{0.5}Ce_{0.5}O_2$ were more reduced than CeO_2, indicating a higher reducibility, consistent with previous studies.[46–48] On the other hand, 50% Gd-doped CeO_2 was less reducible. This could originate from defect–defect interactions in ceria – a high concentration of extrinsic oxygen vacancies and large Gd^{3+} ions increase the formation energy of additional oxygen vacancy (and Ce^{3+}).[49,50]

The amount of the deposited carbon under different biases is shown in ESI Fig. S7b.† Due to voltage loss at the electrolyte and the counter electrode, the applied electrical bias was not entirely converted into an electrochemical potential at the ceria electrodes. Therefore, it is not possible to compare the carbon deposition behavior across samples as a function of bias. Instead, we use the surface reduction state, $[Ce^{3+}]$, as a metric in carbon deposition at the ceria surface. This is reasonable, because $[Ce^{3+}]$ depends on the effective oxygen chemical potential determined by the gas composition and the electrochemical potential at the ceria electrodes.[51] Carbon deposition as a function of $[Ce^{3+}]$ is plotted in Fig. 2b. There are two important features in the $[Ce^{3+}]$-carbon relation: firstly, there is a clear threshold of $[Ce^{3+}]$ for the onset of carbon deposition. As shown on CeO_2 and $Gd_{0.2}Ce_{0.8}O_{1.9}$, significant carbon deposition was only observed when $[Ce^{3+}]$ reached a critical value of around 50%. Secondly, the carbon deposition was suppressed on $Gd_{0.5}Ce_{0.5}O_{1.75}$ and $Zr_{0.5}Ce_{0.5}O_2$. As illustrated, negligible amount of carbon was observed on $Zr_{0.5}Ce_{0.5}O_2$ throughout the entire polarization range even though $[Ce^{3+}]$ exceeded 50%. Although carbon was also observed on $Gd_{0.5}Ce_{0.5}O_{1.75}$ when polarizing the sample to almost 100% $[Ce^{3+}]$, the deposited carbon intensity was much smaller than that on $Gd_{0.2}Ce_{0.8}O_{1.9}$.

Fig. 2c shows the cation fraction of dopants as a function of $[Ce^{3+}]$ during the polarization and carbon deposition process. The surface dopant concentration remained relatively constant before the threshold carbon deposition, but there is an apparent increase after that. For example, the surface Gd concentration in $Gd_{0.2}Ce_{0.8}O_{1.9}$ and $Gd_{0.5}Ce_{0.5}O_{1.75}$ increased at high $[Ce^{3+}]$. The increase of measured cation fraction originates from the fact the XPS signal from Ce gets attenuated more by the deposited carbon, while the dopant are less affected. The observed apparent increase of dopant/Ce ratio thus indicates that more carbon was deposited onto Ce sites than on the dopants (ESI Fig. S12†).

To confirm and better demonstrate the threshold $[Ce^{3+}]$-carbon relation, we monitored carbon deposition on $Gd_{0.2}Ce_{0.8}O_{1.9}$ at different biases (*i.e.*, different $[Ce^{3+}]$) as a function of time. The Ce 4d and C 1s spectra collected during the 1.5 hour measurement at open circuit are shown in Fig. 3a and b respectively. As can be seen, the spectra remained stable throughout the measurement, indicating neither carbon formation nor oxidation state change. Then, a cathodic bias (−0.7 V) was applied to reduce the surface further, but still below the threshold $[Ce^{3+}]$. The spectra collected immediately after polarization, after 0.5 hours and after 1.5 hours are shown in Fig. 3c and d. A small graphitic carbon peak appeared and the surface Ce became more reduced due to cathodic polarization. Nonetheless, no further change of the surface chemistry took place, with no increase in the carbon peak intensity during the 1.5 hours of measurement time. Upon increasing the applied cathode bias to −1.2 V to reduce the surface beyond the $[Ce^{3+}]$ threshold, significant amount of carbon accumulated already within the first 0.5 hours and the carbon intensity continued to increase during the measurement (Fig. 3f). Meanwhile, a new broad peak appeared at about 125 eV, originating from the carbon KVV Auger peak[52] (Fig. 3e). This time-dependent measurement clearly indicates that significant carbon deposition only occurs when the ceria surface reaches a threshold $[Ce^{3+}]$. After the onset of carbon deposition when $[Ce^{3+}]$ was greater than the threshold, the carbon growth exhibited a self-limiting behavior. The carbon intensity at the surface saturated and stopped growing when the thickness of the deposited carbon reached 1–2 monolayers (ESI Note 7†).

Along with the carbon deposition, the adsorbate peak vanished. If indeed this adsorbate is the carbonate precursor in CO_2 electrolysis reaction,[36,38] its suppression indicates loss of catalytic activity for CO_2 electrolysis because of the surface being covered by deposited carbon. In addition, the gas peak shifted to a lower binding energy, possibly due to a change in the gas adsorption behavior on the carbon-covered surface.[53]

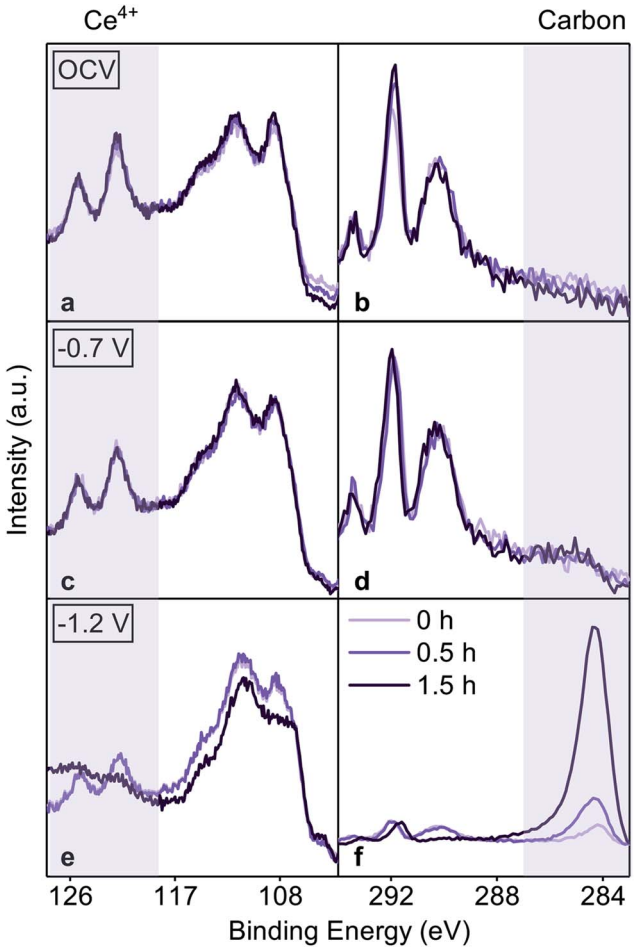

Fig. 3 Time-dependence of carbon deposition on the ceria surface. C 1s and Ce 4d spectra were collected on $Gd_{0.2}Ce_{0.8}O_{1.9}$ at 450 °C in 9 : 1 CO/CO_2 atmosphere at (a and b) open circuit (OCV), (c and d) −0.7 V, and (e and f) −1.2 V electrical bias in sequence. No significant carbon deposition was observed at OCV and −0.7 V, and the surface remained stable during our measurement. Upon reaching the threshold −1.2 V polarization (*i.e.*, threshold $[Ce^{3+}]$), the carbon deposition started and increased sharply. Spectra are normalized to the corresponding CO gas peak.

The change of Ce 4d spectra during carbon deposition is twofold (Fig. 3e): first, the total intensity of the normalized Ce peak decreased as a result of carbon deposition. Second, and more interestingly, the surface became more enriched with Ce^{3+} during carbon deposition. The increase of surface $[Ce^{3+}]$ can be clearly visualized from the decreasing intensity of Ce^{4+} peaks in the Ce 4d spectra by comparing the three spectra in Fig. 3e. Possible reasons for this carbon-induced Ce^{3+} enrichment are discussed in ESI Note 10.†

To summarize, rapid carbon formation from CO only occurred when the surface $[Ce^{3+}]$ exceeded a threshold value of about 50%. This threshold relation is intriguing since the carbon intensity remained negligible prior to the $[Ce^{3+}]$ threshold, despite the considerable amount of Ce^{3+} and $V_o^{\cdot\cdot}$ in the near-surface region. In addition, we found the carbon deposition was almost completely suppressed on both $Gd_{0.5}Ce_{0.5}O_{1.75}$ and $Zr_{0.5}Ce_{0.5}O_2$ throughout the entire polarization range, even after $[Ce^{3+}]$ well exceeded the threshold concentration (50%).

Discussions

We propose that the threshold $[Ce^{3+}]$-carbon relation can have three origins, which may act individually or synergistically. First, the threshold may arise from the thermodynamics aspects ("thermodynamic threshold"), where the carbon deposition reaction is only thermodynamically favorable beyond a threshold cathodic polarization (*i.e.*, threshold $[Ce^{3+}]$). Secondly, the threshold can arise from the formation of catalytic sites for carbon deposition ("catalytic threshold"), where the dominant catalytic sites are only formed in significant numbers beyond a threshold $[Ce^{3+}]$. Thirdly, the threshold may come from the stability of the deposited carbon on the ceria surface ("stability threshold"). For the last case, carbon can be produced at low $[Ce^{3+}]$, but the reaction products stay stably at the ceria surface beyond the threshold of $[Ce^{3+}]$. In the following paragraphs, we discuss all three possibilities and show the threshold $[Ce^{3+}]$-carbon relation must be most likely due to a threshold in the formation of the catalytic structure (Ce^{3+}–Ce^{3+} pair) at the surface ("catalytic threshold").

We first examine the "stability threshold". Ceria is known for its ability to catalyze the combustion of carbon;[54] it may remove (oxidize) the deposited carbon on the surface. As an example, Zr-doped ceria can oxidize the surface carbon with lattice oxygen even at 200 °C.[47] Therefore, it is possible that the deposited carbon can only be stabilized on an oxygen-deficient surface, where no O^{2-} species being available to oxidize the deposited carbon. In this scenario, the observed threshold of $[Ce^{3+}]$ should reflect a threshold of $V_o^{\cdot\cdot}$, where a sufficiently oxygen depleted CeO_2 surface is unable to inhibit carbon deposition. However, this is in contrast to our observation that carbon deposition was suppressed on $Gd_{0.5}Ce_{0.5}O_{1.75}$, the most oxygen-deficient ceria surface at a given $[Ce^{3+}]$. Therefore, we view this scenario to be unlikely.

In addition, the "stability threshold" can originate from a threshold carbon cluster size. Carbon dimers (C_2) have been observed to have higher stability than monomers (C_1) and are the key intermediates in the growth of graphene on Au surfaces.[55] Similarly here, carbon cluster formation may also be a key step in the carbon deposition reaction on ceria. Carbon deposition has been found more favorable near defect sites.[18] Therefore, carbon atoms deposited on the surface with a higher defect concentration are more likely to be located closer to each other, promoting the "clustering" process. In this scenario, the observed threshold $[Ce^{3+}]$-carbon relation should be associated with a threshold surface defect density to ensure that the deposited carbon forms clusters. Clustering of single carbon atoms to form pairs of carbon atoms induces a peak shift in the C 1s spectra as reported by Xu *et al.*[56] We did not find such a peak shift, and therefore we deem this scenario to be unlikely.

We then examine the "thermodynamic threshold". The reaction environment is already thermodynamically favorable for the Boudouard reaction even without polarization.[57] In this

case, a thermodynamic threshold can only arise from the CO dissociation reaction. As the surface [Ce^{3+}] depends directly on the overpotential at the electrode,[51] the threshold [Ce^{3+}]-carbon relation indicates that a threshold of overpotential is required to split the adsorbed CO. Had this scenario been the case, we would expect the surface overpotential to be a good descriptor for the carbon deposition reaction on ceria. In this case, all the samples reported in Fig. 2c should merge into one common threshold overpotential–carbon relation. However, as illustrated in ESI Fig. S17,† this overpotential–carbon relation cannot explain our observation. In particular, this "thermodynamic threshold" cannot resolve the paradox that at similar surface overpotentials, significant amount of carbon deposition was observed on $Gd_{0.2}Ce_{0.8}O_{1.9}$ while nearly no carbon was observed on $Gd_{0.5}Ce_{0.5}O_{1.75}$. Therefore, we assign this scenario to be unlikely as well.

Having excluded the aforementioned scenarios, last but most importantly, we propose that the threshold [Ce^{3+}]-carbon relation should arise from the "catalytic threshold". This means that the catalytic structure can only be effectively formed on the ceria surface beyond a threshold [Ce^{3+}]. Previous studies have assigned either a single site (*i.e.*, individual Ce^{3+} site[58] or $V_o^{\cdot\cdot}$ (ref. 18)) or a neighboring pair of sites (*i.e.*, Ce^{3+}–Ce^{4+} pair[17]) as the catalytic structures for carbon deposition from CO on ceria and other oxides. From our observation, we can already exclude the case of single sites. Had the dominant catalytic structure been a single Ce^{3+} or $V_o^{\cdot\cdot}$ site, the deposited carbon should have increased progressively with [Ce^{3+}] rather than exhibiting a threshold onset. Therefore, we constrain our following discussion to the neighboring defect pairs. As redox-inert Zr and Gd sites don't participate in the reaction,[59] five types of surface defect pairs may act as the catalytic structure: Ce^{3+}–Ce^{4+} pair, Ce^{3+}–Ce^{3+} pair, Ce^{3+}–O pair, Ce^{3+}–$V_o^{\cdot\cdot}$ pair, and Ce^{4+}–$V_o^{\cdot\cdot}$ pair. Meanwhile, despite the difference in the nominal oxygen vacancy concentration at a given [Ce^{3+}], similar [Ce^{3+}]-carbon relations have been observed between CeO_2 and $Gd_{0.2}Ce_{0.8}O_{1.9}$; and between $Zr_{0.5}Ce_{0.5}O_2$ and $Gd_{0.5}Ce_{0.5}O_{1.75}$, indicating that both the oxygen sites and the $V_o^{\cdot\cdot}$ play a minor role, if any, in catalyzing carbon deposition. Consequently, only the Ce pairs (Ce^{3+}–Ce^{4+} or Ce^{3+}–Ce^{3+}) may act as the catalytic structure.

To resolve the most likely catalytic structure, we conducted a model Metropolis Monte Carlo simulation to quantify Ce pair formation on the ceria surface as a function of [Ce^{3+}]. In principle, one would need to consider all the possible surface terminations to model site-by-site the pairing of reduced ceria cations. Here, we model the Ce^{3+} pair formation on the (001)-type ceria surface, *i.e.*, the majority surface structure of the electrochemical cell. As will be presented later, the insights drawn from the (001) surface model can be extended to other types of ceria facets as well. Different energies of defect–defect interactions between the nearest-neighbor Ce^{3+} sites ($E_{Ce^{3+}-Ce^{3+}}$) were tested, ranging from 0 to 0.2 eV, with positive values representing repulsion. The energies were chosen from a previous calculation, indicating the interaction energy between the nearest-neighbor Ce^{3+}–Ce^{3+} pair in the bulk of ceria is 0.1 eV.[60] As a result, Fig. 4a shows the concentration of Ce^{3+}–Ce^{4+} and Ce^{3+}–Ce^{3+} pairs on the equilibrated undoped lattice at different

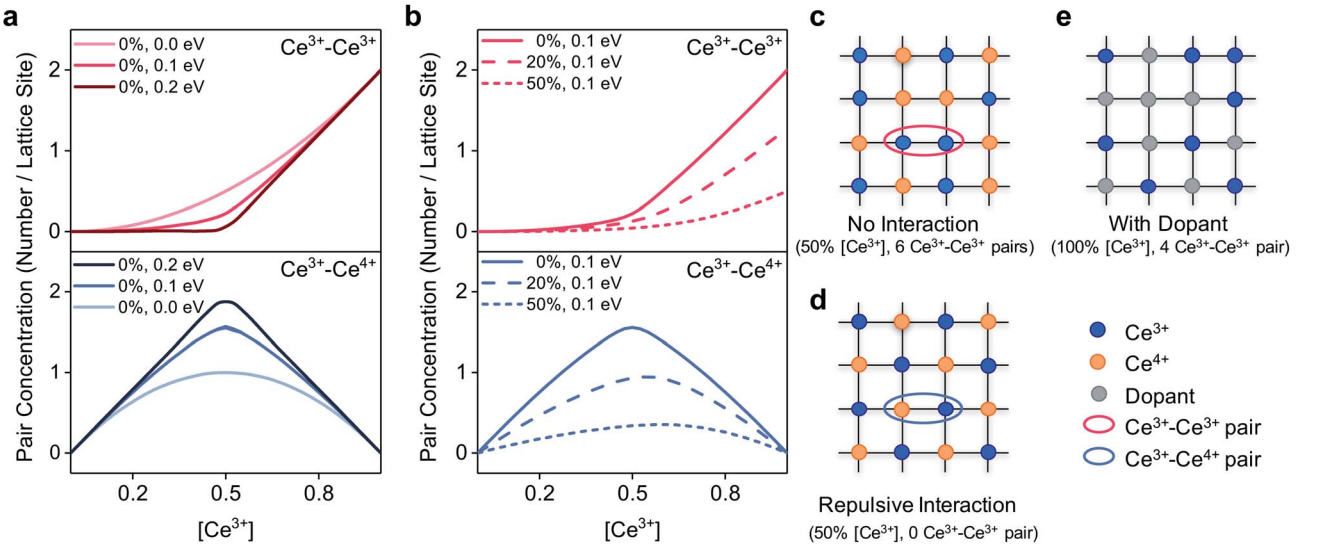

Fig. 4 Quantification of Ce pair formation on the (001) ceria surface with Monte Carlo simulation. (a) The response of Ce pair formation to the interaction energy between neighboring Ce^{3+} cations, with positive energies representing repulsion. Note a threshold behavior was observed in the Ce^{3+}–Ce^{3+} pair formation at repulsive interaction energies, and no threshold is found for the formation of Ce^{3+}–Ce^{4+} pairs, as expected. (b) Effect of doping on the Ce pair concentration, with the interaction energy fixed at 0.1 eV. Note that doping suppresses Ce pair formation. The error bar for the simulation is smaller than the line width. (c–e) Exemplify three scenario, with schematic lattices showing the effect of repulsive interaction and doping on the Ce^{3+} pair formation: (c) undoped ceria surface without neighboring Ce^{3+} pair interaction, where Ce^{3+} and Ce^{4+} arrange randomly. (d) Undoped ceria surface with repulsive Ce^{3+}–Ce^{3+} interaction. Since Ce^{3+} and Ce^{4+} arrange alternatingly, no Ce^{3+}–Ce^{3+} pair is formed up to 50% [Ce^{3+}]. (e) Ceria lattice with 50% of its sites occupied by the dopant. Since Ce sites are isolated from each other by the dopants, the Ce^{3+}–Ce^{3+} pair formation is suppressed.

interaction energies. When $E_{Ce^{3+}-Ce^{3+}} = 0$ eV (no interaction), the concentration of Ce^{3+}–Ce^{3+} pairs progressively increased with [Ce^{3+}]. However, when considering the repulsive interactions ($E_{Ce^{3+}-Ce^{3+}} = 0.1$, 0.2 eV), a threshold formation of Ce^{3+}–Ce^{3+} pair appeared. On the other hand, no threshold relation was found in the formation of Ce^{3+}–Ce^{4+} pairs, as expected.

The effect of doping on Ce pair formation is shown in Fig. 4b, with the interaction energy between neighboring Ce^{3+} sites fixed at 0.1 eV.[60] As described in more detail in the Methods section, the dopant sites are randomly distributed and are treated as immobile during the simulation. Lattices with three different doping ratios were calculated: 0%, 20%, and 50%, which is in accord with the surface composition measured with APXPS (Fig. 2c). As a result, lattices with higher doping ratio exhibited a smaller concentration of Ce^{3+}–Ce^{4+} and Ce^{3+}–Ce^{3+} pairs.

The dependence of Ce pair concentrations on the interaction energy and doping concentration is explained as follows. Due to the repulsive interactions between adjacent Ce^{3+} sites, it is energetically more favorable for Ce^{3+} to be surrounded by Ce^{4+} (Fig. 4d). As a result, the Ce^{3+}–Ce^{3+} pair is difficult to form at low [Ce^{3+}]. However, once [Ce^{3+}] exceeds 50%, any increase in [Ce^{3+}] results in additional Ce^{3+}–Ce^{3+} pair formation because of site unavailability, regardless of the interaction strength. Consequently, the Ce^{3+}–Ce^{3+} pair concentration exhibits a threshold formation against [Ce^{3+}]. Regarding the doping effect: since dopants were treated as immobile sites between Ce atoms in the lattice, they impede Ce^{3+}–Ce^{3+} pair formation by "isolating" Ce sites from each other (Fig. 4e). Note each lattice structure shown in Fig. 4c–e only represents one possible configuration at a given [Ce^{3+}] and dopant concentration. In the real simulation process, a 50 by 50 2D cubic lattice was employed and the simulation results in Fig. 4a and b reflect the average values obtained from energy minimization of different lattice configurations.

As demonstrated in the Monte Carlo simulations, the catalysis of carbon deposition reaction is very likely linked to the Ce^{3+}–Ce^{3+} pair formation. To better verify this idea, Fig. 5 presents the comparison of the carbon deposition measured by APXPS and the calculated Ce^{3+}–Ce^{3+} pair concentration. The simulated Ce^{3+}–Ce^{3+} pair formation exhibits a very similar behavior as the deposited carbon intensity as a function of [Ce^{3+}]: the model not only captures the absolute value of the onset threshold (~50% [Ce^{3+}]) but also correctly reflects the relative carbon intensity between ceria surfaces at different doping concentrations. As a result, we conclude that our model qualitatively delivers a strong evidence that the neighboring Ce^{3+}–Ce^{3+} pair is the corresponding catalytic structure for carbon deposition from CO. Even though we modeled the pairing effect on the (001) surface, we believe that the same argument can be also applicable to other major surface terminations. This is because, regardless of the surface termination, two CO molecules must be dissociated nearby to each other, to enable the C–C bond formation during the growth of graphitic carbon. In other words, it is the formation of adjacent catalytic sites for carbon deposition, *i.e.*, the formation of a nearest neighbor "Ce^{3+}–Ce^{3+} pair", that is critical for the coking reaction. Since the distance between the nearest Ce–Ce pairs is the same on the (001), (011), and (111) fluorite-type surfaces, we would expect a similar catalytic behavior for carbon deposition on these low-index surface terminations of ceria. Nevertheless, future studies are needed to confirm this.

To summarize, in this section we discussed three possible origins of the onset of carbon deposition at a threshold [Ce^{3+}] at ceria surfaces. We deduce that this behavior arises most likely because of the formation of Ce^{3+}–Ce^{3+} pairs after exceeding a threshold of [Ce^{3+}] at the surface. From this, we also deduce that the Ce^{3+}–Ce^{3+} pair serves as the catalytic structure for carbon deposition from CO. Consistent with this argument, the enhanced

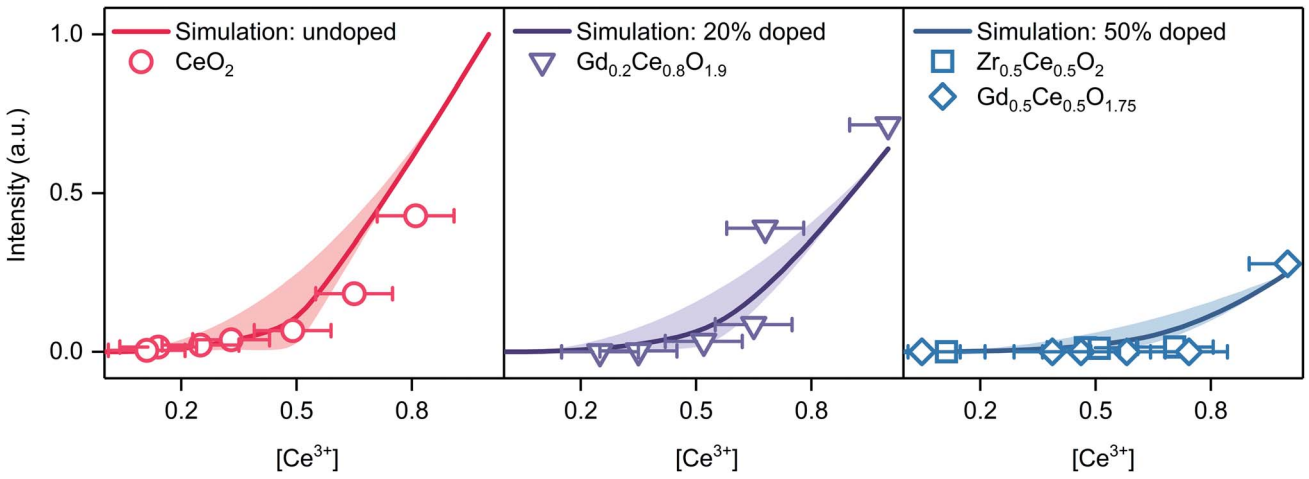

Fig. 5 Comparison between the measured carbon deposition and the simulated Ce^{3+}–Ce^{3+} pair formation, as a function of [Ce^{3+}]. The calculated Ce^{3+}–Ce^{3+} pair density (line) and the measured carbon intensity (points) are in good overall agreement. Note the model captures the threshold onset and the doping effect, supporting the theory that the neighboring Ce^{3+}–Ce^{3+} pair is the catalytic structure for carbon deposition from CO. All the simulation curves were replotted from Fig. 4b and divided by a common normalization factor to ease comparison. The solid lines represent the Ce^{3+}–Ce^{3+} pair density calculated with 0.1 eV interaction energy, whereas the shaded regions indicate the variations when changing the interaction energy from 0 eV to 0.2 eV.

carbon resistance on 50% Zr-doped and 50% Gd-doped ceria originates from a suppressed Ce^{3+}–Ce^{3+} pair formation. In this work, the proposed catalytic structure does not define a specific reaction pathway, and further studies are needed to reveal the atomistic reaction steps enabled by this catalytic structure.

Conclusions

In this work, we systematically studied the carbon deposition reaction during CO_2 electrolysis on four fluorite-type ceria thin films: CeO_2, $Gd_{0.2}Ce_{0.8}O_{1.9}$, $Gd_{0.5}Ce_{0.5}O_{1.75}$, and $Zr_{0.5}Ce_{0.5}O_2$. By performing *in operando* APXPS measurements, we revealed that, despite the general opinion that CeO_2 is a carbon-tolerant catalyst, carbon deposition can readily occur on CeO_2 surfaces in LT-SOCs conditions. This observation clearly highlights the importance of investigating carbon deposition on CeO_2 surfaces to mitigate carbon poisoning in LT-SOCs. Moreover, carbon deposition exhibits an onset at a threshold value of 50% Ce^{3+} concentration when dopant concentration is relatively low or zero. This intriguing threshold [Ce^{3+}]-carbon relation deepens the understanding of the carbon deposition reaction mechanism: combining APXPS data with Monte Carlo simulation, we propose the most likely catalytic structure for carbon deposition to be the neighboring Ce^{3+}–Ce^{3+} pair. Inspired by this mechanism, we propose that doping CeO_2 with non-redox-active cations can effectively mitigate the carbon deposition on CeO_2 under LT-SOC operating conditions. This idea has been verified with *in operando* APXPS on 50% Gd and 50% Zr-doped CeO_2, where carbon formation has been effectively suppressed.

Since Ce^{3+} is a key enabler in a wide range of electrocatalytic reactions,[24,36] suppressing carbon deposition while maintaining a high [Ce^{3+}] is required for developing carbon-tolerant ceria-based electrocatalysts. Our results indicate that suppressing Ce^{3+}–Ce^{3+} pair formation at high [Ce^{3+}] can be the key to alleviate carbon deposition from CO. This includes ways to isolate Ce^{3+} cations from each other, for example by doping ceria with non-redox-active cations (such as 50% Zr- and 50% Gd-doped CeO_2 in this work). When used as fuel cell electrodes, it has been suggested that higher Gd concentrations in Gd-doped ceira can improve electrode's electrical conductivity as well as dimensional stability.[61] Previous studies have also shown that heavily Zr-doped ceria benefits oxygen surface exchange[62] as well as bulk diffusivity.[63] Therefore, both enhanced carbon resistance and electrocatalytic performance could be realized simultaneously on heavily doped ceria surfaces. In addition, as the number of Ce^{3+} sites per unit surface area of doped ceria is lower than the undoped case, one may also consider increasing the total surface area of the doped ceria by employing nanoparticles.[64,65]

Methods

Film fabrication

The electrochemical cells were fabricated on 10 mm × 10 mm × 0.5 mm 8% yttria-stabilized zirconia (YSZ) (001) single crystal substrates (MTI Corporation), which served as the solid electrolyte. Pt paste (SPI Supplies) was applied on the back of the YSZ substrate and then sintered in air at 800 °C for 1 hour as the counter electrode (CE). Buried, micro-patterned Pt grids were fabricated through photolithography on the front side of the substrate as the current collector (ESI Fig. S1†). The thin film working electrode (WE) was deposited on top of YSZ and Pt grids using pulsed laser deposition (PLD), where a KrF excimer laser with 248 nm wavelength was used. During deposition, the substrate temperature was kept at 750 °C in an oxygen pressure of 10 mTorr.

In operando APXPS

The APXPS measurements were carried out at Beamline 9.3.2 of the Advanced Light Source, Lawrence Berkeley National Laboratory (ALS); the NAP-XPS end station of the Pierre and Marie Curie University set on TEMPO beamline at Synchrotron SOLEIL; and the IOS beamline 23-ID-2 of the National Synchrotron Light Source II (NSLS-II) at Brookhaven National Lab. The electrochemical cells described above were placed on a ceramic heater, with thermocouples mounted directly onto the surface for temperature measurements. The thermocouple along with a Pt wire was also used to apply electrochemical bias on the sample, where the Pt wire was welded to a Pt foil beneath the CE. During the experiment, cathodic (CO_2 reduction) and anodic (CO oxidation) biases were applied on the electrochemical cell to drive surface redox reaction as well as to change the oxidation state of surface Ce cations.

Samples were preconditioned at 350 °C in 20 mTorr O_2 at the beginning of the measurement to remove adventitious carbon. The *operando* environment studied in this work was 450 °C in 0.15 Torr (SOLEIL, NSLS-II) and 0.3 Torr (ALS) 9 : 1 CO/CO_2 atmosphere, under cell bias ranging from +0.7 to −1.5 V. The APXPS spectra were collected at an incident photon energy of 370 eV (SOLEIL) and 400 eV (ALS, NSLS-II). CeO_2, $Gd_{0.5}Ce_{0.5}O_{1.75}$, and $Zr_{0.5}Ce_{0.5}O_2$ were tested in ALS while $Gd_{0.2}Ce_{0.8}O_{1.9}$ were tested in all of the three beamlines.

All the XPS spectra were quantified with CasaXPS software. Carbon deposition intensity was calculated by integrating the graphitic carbon area in the C 1s spectra and then normalized to the CO gas peak intensity (ESI Note 4†). [Ce^{3+}] was calculated as the peak area ratio of Ce^{3+} features to the total area of Ce 4d (ESI Note 5†).

Monte Carlo simulation

A 50 × 50 2D square lattice with periodic boundary conditions was employed to simulate the ceria (001) surface. Since the aim of this simulation is to quantify Ce pair formation, the simulated lattice consists purely of Ce and dopant sites, and no oxygen sites were considered. In the simulated square 2D lattice, each atom has four nearest neighboring sites and represents either a Ce (Ce^{3+} or Ce^{4+}) or a dopant. Only the interaction between two nearest Ce^{3+} sites was considered, while all other interactions were ignored. Therefore, the system Hamiltonian can be expressed as $H = N_{Ce^3\text{–}Ce^3} \cdot E_{Ce^3\text{–}Ce^3}$, where $N_{Ce^3\text{–}Ce^3}$ and $E_{Ce^3\text{–}Ce^3}$ denote the Ce^{3+}–Ce^{3+} pair number and the interaction energy between them, respectively. In this model, Ce^{3+} and Ce^{4+} sites were set free to switch while dopant sites were considered immobile. This assumption is in agreement

with the significant lower mobility of cations compared to that of polarons in ceria.[66] The Metropolis Monte Carlo simulation was conducted as follows:

(1) Randomly pick two Ce sites on the lattice and calculate the energy difference ΔH of switching Ce^{3+} and Ce^{4+}.

(2) If the switch results in a reduced system energy ($\Delta H < 0$), accept it with a probability of 1. Otherwise, accept the switch with a probability of exp ($\Delta H/k_BT$), where k_B and T denote the Boltzmann constant and temperature respectively.

In accord with the experimental environment, the simulation temperature was set to be 450 °C. 100 random configurations were generated as initial guesses at each [Ce^{3+}] and doping ratio. Then each of the 100 initial lattices was evolved by switching sites according to the Metropolis scheme. Each Monte Carlo step (MCS) consisted of 2500 switching trials, and the ensemble average was estimated by averaging over the last 200 MCS after equilibrium. Finally, the concentration of Ce pairs (both Ce^{3+}–Ce^{3+} and Ce^{3+}–Ce^{4+}) were calculated as the mean value of the 100 thermodynamically equilibrated lattices (ESI Note 11†).

Author contributions

J. W., S. R. B., and B. Y. conceived the experiment design. J. W. and Q. L. prepared the samples and J. W. conducted the sample characterization. All authors carried out the APXPS experiments. J. W. performed the Monte Carlo simulations. All authors contributed to writing the manuscript. B. Y. supervised the project.

Conflicts of interest

The authors declare that they have no competing financial interests.

Acknowledgements

The authors are grateful for the funding support from the National Aeronautics and Space Administration in support of the Mars Oxygen ISRU Experiment (award number NNH17CH01C), and from Exelon Corp (award number 025610-00007). The authors acknowledge the facility support from the Microsystems Technology Laboratories and the Center for Materials Science and Engineering (NSF under award number DMR-1419807) at MIT. This research used the synchrotron radiation facilities at the National Synchrotron Light Source II (23-ID-2 beamline), a U.S. Department of Energy (DOE) Office of Science User Facility operated for the DOE Office of Science by Brookhaven National Laboratory under Contract No. DE-SC0012704; the Advanced Light Source which is supported by the DOE Office of Basic Energy Sciences under Contract No. DE-AC02-05CH11231; and the TEMPO beamline at the Synchrotron SOLEIL. The authors thank Peter A. Crozier (ASU), William Chueh (Stanford), Ulrike Diebold, Alexander K. Opitz (TU Wien) and Franziska Hess (MIT) for the helpful discussions on the carbon deposition reaction mechanisms. The authors also thank Dongha Kim (MIT) and Maximilian Jansen (ETH) for the assistance of APXPS measurement. J. W. and B. Y. thank Dr Rachael Rothman (University of Sheffield) for her helpful advice and input on the preparation of this manuscript. J. W. thanks Hongzhou Ye and Charles Settens (MIT) for the helpful discussions on the Monte Carlo simulation and XRD measurements.

References

1 A. Schoedel, Z. Ji and O. M. Yaghi, The role of metal–organic frameworks in a carbon-neutral energy cycle, *Nat. Energy*, 2016, **1**, 16034.
2 C. Graves, S. D. Ebbesen, M. Mogensen and K. S. Lackner, Sustainable hydrocarbon fuels by recycling CO_2 and H_2O with renewable or nuclear energy, *Renewable Sustainable Energy Rev.*, 2011, **15**, 1–23.
3 K. Chen and S. P. Jiang, Reviewmaterials degradation of solid oxide electrolysis cells, *J. Electrochem. Soc.*, 2016, **163**, F3070–F3083.
4 J. R. Scheffe and A. Steinfeld, Oxygen exchange materials for solar thermochemical splitting of H_2O and CO_2: a review, *Mater. Today*, 2014, **17**, 341–348.
5 Z. Gao, L. V. Mogni, E. C. Miller, J. G. Railsback and S. A. Barnett, A perspective on low-temperature solid oxide fuel cells, *Energy Environ. Sci.*, 2016, **9**, 1602–1644.
6 L. Fan, B. Zhu, P.-C. Su and C. He, Nanomaterials and technologies for low temperature solid oxide fuel cells: Recent advances, challenges and opportunities, *Nano Energy*, 2018, **45**, 148–176.
7 D. Neagu, *et al.*, Nano-socketed nickel particles with enhanced coking resistance grown *in situ* by redox exsolution, *Nat. Commun.*, 2015, **6**, 8120.
8 B. Liu, *et al.*, Microwaves effectively examine the extent and type of coking over acid zeolite catalysts, *Nat. Commun.*, 2017, **8**, 514.
9 P. Boldrin, *et al.*, Strategies for carbon and sulfur tolerant solid oxide fuel cell materials, incorporating lessons from heterogeneous catalysis, *Chem. Rev.*, 2016, **116**, 13633–13684.
10 S. R. Bishop, *et al.*, Oxygen generation from carbon dioxide for advanced life support, *ECS Trans.*, 2008, **11**, 173–179.
11 S. D. Ebbesen and M. Mogensen, Electrolysis of carbon dioxide in solid oxide electrolysis cells, *J. Power Sources*, 2009, **193**, 349–358.
12 M. P. Kohn, M. J. Castaldi and R. J. Farrauto, Auto-thermal and dry reforming of landfill gas over a Rh/AL_2O_3 monolith catalyst, *Appl. Catal., B*, 2010, **94**, 125–133.
13 J. Harmsen, W. Jansen, J. Hoebink, J. Schouten and H. Brongersma, Coke deposition on automotive three-way catalysts studied with leis, *Catal. Lett.*, 2001, **74**, 133–137.
14 A. Goguet, *et al.*, Study of the origin of the deactivation of a Pt/CeO_2 catalyst during reverse water gas shift (rwgs) reaction, *J. Catal.*, 2004, **226**, 382–392.
15 J.-X. Liu, B.-Y. Zhang, P.-P. Chen, H.-Y. Su and W.-X. Li, CO dissociation on face-centered cubic and hexagonal close-packed nickel catalysts: A first-principles study, *J. Phys. Chem. C*, 2016, **120**, 24895–24903.

16 E. Putna, R. Gorte, J. Vohs and G. Graham, Evidence for enhanced dissociation of CO on Rh/ceria, *J. Catal.*, 1998, **178**, 598–603.
17 Y. Liu, *et al.*, Mechanism of CO disproportionation on reduced ceria, *ChemCatChem*, 2010, **2**, 336–341.
18 M. Kogler, *et al.*, High-temperature carbon deposition on oxide surfaces by CO disproportionation, *J. Phys. Chem. C*, 2016, **120**, 1795–1807.
19 G. M. Bremmer, *et al.*, *In situ* tem observation of the boudouard reaction: multi-layered graphene formation from co on cobalt nanoparticles at atmospheric pressure, *Faraday Discuss.*, 2017, **197**, 337–351.
20 K. Girona, J. Laurencin, J. Fouletier and F. Lefebvre-Joud, Carbon deposition in CH_4/CO_2 operated sofc: Simulation and experimentation studies, *J. Power Sources*, 2012, **210**, 381–391.
21 J. A. Rodriguez, D. C. Grinter, Z. Liu, R. M. Palomino and S. D. Senanayake, Ceria-based model catalysts: fundamental studies on the importance of the metal-ceria interface in CO oxidation, the water-gas shift, CO_2 hydrogenation, and methane and alcohol reforming, *Chem. Soc. Rev.*, 2017, **46**, 1824–1841.
22 T. Montini, M. Melchionna, M. Monai and P. Fornasiero, Fundamentals and catalytic applications of CeO_2-based materials, *Chem. Rev.*, 2016, **116**, 5987–6041.
23 W. C. Chueh, Y. Hao, W. Jung and S. M. Haile, High electrochemical activity of the oxide phase in model ceria–Pt and ceria–Ni composite anodes, *Nat. Mater.*, 2012, **11**, 155–161.
24 W. C. Chueh, *et al.*, Highly enhanced concentration and stability of reactive Ce^{3+} on doped CeO_2 surface revealed in operando, *Chem. Mater.*, 2012, **24**, 1876–1882.
25 H. L. Tuller and S. R. Bishop, Point defects in oxides: Tailoring materials through defect engineering, *Annu. Rev. Mater. Res.*, 2011, **41**, 369–398.
26 H. Tuller and A. Nowick, Small polaron electron transport in reduced CeO_2 single crystals, *J. Phys. Chem. Solids*, 1977, **38**, 859–867.
27 E. L. Lawrence and P. A. Crozier, Oxygen transfer at metal-reducible oxide nanocatalyst interfaces: Contrasting carbon growth from ethane and ethylene, *ACS Appl. Nano Mater.*, 2018, **1**, 1360–1369.
28 V. Duboviks, *et al.*, A raman spectroscopic study of the carbon deposition mechanism on Ni/CGO electrodes during CO/CO2 electrolysis, *Phys. Chem. Chem. Phys.*, 2014, **16**, 13063–13068.
29 Y. Lin, Z. Zhan, J. Liu and S. A. Barnett, Direct operation of solid oxide fuel cells with methane fuel, *Solid State Ionics*, 2005, **176**, 1827–1835.
30 W. Li, Y. Shi, Y. Luo, Y. Wang and N. Cai, Carbon deposition on patterned nickel/yttria stabilized zirconia electrodes for solid oxide fuel cell/solid oxide electrolysis cell modes, *J. Power Sources*, 2015, **276**, 26–31.
31 T. L. Skafte, P. Blennow, J. Hjelm and C. Graves, Carbon deposition and sulfur poisoning during CO_2 electrolysis in nickel-based solid oxide cell electrodes, *J. Power Sources*, 2018, **373**, 54–60.
32 T. L. Skafte, C. Graves, P. Blennow and J. Hjelm, Carbon deposition during CO_2 electrolysis in ni-based solid-oxide-cell electrodes, *ECS Trans.*, 2015, **68**, 3429–3437.
33 H. Kan and H. Lee, Enhanced stability of NiFe/GDC solid oxide fuel cell anodes for dry methane fuel, *Catal. Commun.*, 2010, **12**, 36–39.
34 V. F. Solovyov, *et al.*, Highly efficient solid state catalysis by reconstructed (001) ceria surface, *Sci. Rep.*, 2014, **4**, 4627.
35 D. Mullins, S. Overbury and D. Huntley, Electron spectroscopy of single crystal and polycrystalline cerium oxide surfaces, *Surf. Sci.*, 1998, **409**, 307–319.
36 Z. A. Feng, M. L. Machala and W. C. Chueh, Surface electrochemistry of CO_2 reduction and CO oxidation on Sm-doped CeO_2-x: coupling between Ce^{3+} and carbonate adsorbates, *Phys. Chem. Chem. Phys.*, 2015, **17**, 12273–12281.
37 Z. Liu, *et al.*, Ambient pressure XPS and IRRAS investigation of ethanol steam reforming on Ni-CeO_2(111) catalysts: an *in situ* study of C–C and O–H bond scission, *Phys. Chem. Chem. Phys.*, 2016, **18**, 16621–16628.
38 Y. Yu, *et al.*, CO_2 activation and carbonate intermediates: an operando AP-XPS study of CO_2 electrolysis reactions on solid oxide electrochemical cells, *Phys. Chem. Chem. Phys.*, 2014, **16**, 11633–11639.
39 T. Staudt, *et al.*, Electronic structure of magnesia ceria model catalysts, CO_2 adsorption, and CO_2 activation: A synchrotron radiation photoelectron spectroscopy study, *J. Phys. Chem. C*, 2011, **115**, 8716–8724.
40 M. Favaro, *et al.*, Subsurface oxide plays a critical role in CO_2 activation by Cu(111) surfaces to form chemisorbed CO_2, the first step in reduction of CO_2, *Proc. Natl. Acad. Sci. U. S. A.*, 2017, **114**, 6706–6711.
41 S. Chen, *et al.*, Probing surface structures of CeO_2, TiO_2, and Cu_2O nanocrystals with CO and CO_2 chemisorption, *J. Phys. Chem. C*, 2016, **120**, 21472–21485.
42 S. Blomberg, *et al.*, *Phys. Rev. Lett.*, 2013, **110**, 117601.
43 B. Eren, C. Heine, H. Bluhm, G. A. Somorjai and M. Salmeron, Catalyst chemical state during CO oxidation reaction on Cu(111) studied with ambient-pressure X-ray photoelectron spectroscopy and near edge X-ray adsorption fine structure spectroscopy, *J. Am. Chem. Soc.*, 2015, **137**, 11186–11190.
44 C. Zhang, *et al.*, Multielement activity mapping and potentiacs catalysisal mapping in solid oxide electrochemical cells through the use of operando XPS, *ACS Catal.*, 2012, **2**, 2297–2304.
45 Z. A. Feng, F. El Gabaly, X. Ye, Z.-X. Shen and W. C. Chueh, Fast vacancy-mediated oxygen ion incorporation across the ceria–gas electrochemical interface, *Nat. Commun.*, 2014, **5**, 4374.
46 S. Grieshammer, M. Nakayama and M. Martin, Association of defects in doped non-stoichiometric ceria from first principles, *Phys. Chem. Chem. Phys.*, 2016, **18**, 3804–3811.
47 E. Aneggi, *et al.*, Ceriazirconia particles wrapped in a 2D carbon envelope: Improved low temperature oxygen transfer and oxidation activity, *Angew. Chem., Int. Ed.*, 2015, **54**, 14040–14043.

48 S. Bishop, K. Duncan and E. Wachsman, Defect equilibria and chemical expansion in non-stoichiometric undoped and gadolinium-doped cerium oxide, *Electrochim. Acta*, 2009, **54**, 1436–1443.

49 S. R. Bishop, T. S. Stefanik and H. L. Tuller, Electrical conductivity and defect equilibria of $Pr_{0.1}Ce_{0.9}O_2$-δ, *Phys. Chem. Chem. Phys.*, 2011, **13**, 10165–10173.

50 C. Chatzichristodoulou and P. V. Hendriksen, Oxygen nonstoichiometry and defect chemistry modeling of $Ce_{0.8}Pr_{0.2}O_2$, *J. Electrochem. Soc.*, 2010, **157**, B481–B489.

51 D. Chen and H. L. Tuller, Voltagecontrolled nonstoichiometry in oxide thin films: $Pr_{0.1}Ce_{0.9}O_2$ case study, *Adv. Funct. Mater.*, 2014, **24**, 7638–7644.

52 J. S. Murday, B. I. Dunlap, F. L. Hutson and P. Oelhafen, Carbon KVV auger line shapes of graphite and stage-one cesium and lithium intercalated graphite, *Phys. Rev. B*, 1981, **24**, 4764–4770.

53 S. Porsgaard, *et al.*, Charge state of gold nanoparticles supported on titania under oxygen pressure, *Angew. Chem., Int. Ed.*, 2011, **50**, 2266–2269.

54 E. Ramírez-Cabrera, A. Atkinson and D. Chadwick, The influence of point defects on the resistance of ceria to carbon deposition in hydrocarbon catalysis, *Solid State Ionics*, 2000, **136–137**, 825–831.

55 S. Riikonen, A. V. Krasheninnikov, L. Halonen and R. M. Nieminen, The role of stable and mobile carbon adspecies in copper-promoted graphene growth, *J. Phys. Chem. C*, 2012, **116**, 5802–5809.

56 L. Xu, *et al.*, Transformation of carbon monomers and dimers to graphene islands on CO(0001): Thermodynamics and kinetics, *J. Phys. Chem. C*, 2013, **117**, 2952–2958.

57 K. Sasaki and Y. Teraoka, Equilibria in fuel cell gases: Ii. the C–H–O ternary diagrams, *J. Electrochem. Soc.*, 2003, **150**, A885–A888.

58 M. Swanson, V. V. Pushkarev, V. I. Kovalchuk and J. L. d'Itri, The dynamic surface chemistry during the interaction of CO with ceria captured by raman spectroscopy, *Catal. Lett.*, 2007, **116**, 41–45.

59 J. Paier, C. Penschke and J. Sauer, Oxygen defects and surface chemistry of ceria: Quantum chemical studies compared to experiment, *Chem. Rev.*, 2013, **113**, 3949–3985.

60 S. Grieshammer and M. Martin, Influence of defect interactions on the free energy of reduction in pure and doped ceria, *J. Mater. Chem. A*, 2017, **5**, 9241–9249.

61 R. O'hayre, S.-W. Cha, F. B. Prinz and W. Colella, *Fuel Cell Fundamentals*, John Wiley & Sons, 2016.

62 N. Yang, *et al.*, Role of associated defects in oxygen ion conduction and surface exchange reaction for epitaxial samaria-doped ceria thin films as catalytic coatings, *ACS Appl. Mater. Interfaces*, 2016, **8**, 14613–14621.

63 T. Wakita and M. Yashima, Structural disorder in the cubic $Ce_{0.5}Zr_{0.5}O_2$ catalyst: A possible factor of the high catalytic activity, *Appl. Phys. Lett.*, 2008, **92**, 101921.

64 J.-h. Myung, D. Neagu, D. N. Miller and J. T. Irvine, Switching on electrocatalytic activity in solid oxide cells, *Nature*, 2016, **537**, 528.

65 Y. Chen, *et al.*, A robust and active hybrid catalyst for facile oxygen reduction in solid oxide fuel cells, *Energy Environ. Sci.*, 2017, **10**, 964–971.

66 S. Beschnitt, T. Zacherle and R. A. De Souza, Computational study of cation diffusion in ceria, *J. Phys. Chem. C*, 2015, **119**, 27307–27315.